One-Dimensional Photonic Bandgap Microcavities for Strong Optical Confinement in GaAs and $GaAs/Al_xO_y$ Semiconductor Waveguides

Daniel J. Ripin, Kuo-Yi Lim, *Member, IEEE, Member, OSA,* G. S. Petrich, *Member, IEEE,* Pierre R. Villeneuve, *Member, OSA,* Shanhui Fan, *Member, OSA,* E. R. Thoen, *Student Member, IEEE, Student Member, OSA,* John D. Joannopoulos, E. P. Ippen, *Fellow, IEEE, Fellow, OSA,* and L. A. Kolodziejski, *Senior Member, IEEE, Member, OSA*

***Abstract*— Photonic bandgap (PBG) waveguide microcavities with tightly confined resonant optical modes have been designed, fabricated using high-dielectric-contrast $GaAs/Al_xO_y$ III–V compound semiconductor structures, and characterized optically. The photonic crystal lattices are defined by one-dimensional (1-D) arrays of holes in waveguides, and a controlled defect in the spacing between two holes of an array defines a microcavity. Waveguide microcavity resonances have been studied in both monorail and suspended air-bridge geometries. Resonance states with cavity Q's as high as 360 were measured at wavelengths near 1.55 μm, with modal volumes as small as 0.026 μm^3, which corresponds to only two times $(\lambda/2n)^3$.**

***Index Terms*—Gallium alloys, nanotechnology, optical materials, optical waveguide filters, optical waveguide theory, semiconductor waveguides.**

I. Introduction

THE confinement of light to small volumes has important consequences for the properties of optical emission within the region of light confinement. The density of electromagnetic states inside a cavity is significantly modified, and the spontaneous emission of atoms in a cavity can be either enhanced or inhibited. Highly confined optical systems can therefore be used to reduce the size and power requirements of integrated optical components, to generate single-mode operation of light-emitting devices, to reduce the lasing threshold of semiconductor lasers, and to allow higher modulation speeds of these devices [1].

Manuscript received April 9, 1999; revised August 17, 1999. This work was supported in part by the MRSEC program of the National Science Foundation under Award DMR-9400334 and in part by the ARO under contracts DAAGSS-98-1-0080 and DAAH04-93-G-0262.

D. J. Ripin, P. R. Villeneuve, S. Fan, and J. D. Joannopoulos are with the Department of Physics, Research Laboratory of Electronics, Center for Materials Science and Engineering, Massachusetts Institute of Technology, Cambridge, MA 02139-4307 USA.

K.-Y. Lim, G. S. Petrich, E. R. Thoen, and L. A. Kolodziejski are with the Department of Electrical Engineering and Computer Science, Research Laboratory of Electronics, Center for Materials Science and Engineering, Massachusetts Institute of Technology, Cambridge, MA 02139-4307 USA.

E. P. Ippen is with the Department of Physics and the Department of Electrical Engineering and Computer Science, Research Laboratory of Electronics, Center for Materials Science and Engineering, Massachusetts Institute of Technology, Cambridge, MA 02139-4307 USA.

Publisher Item Identifier S 0733-8724(99)08806-4.

Photonic bandgap (PBG) materials, also known as photonic crystals, offer a method of achieving strong photon confinement to volumes on the order of $(\lambda/2n)^3$, where λ is the photon wavelength and n is the refractive index of the host material [2], [3]. Highly confined optical states arise from the introduction of local defects inside photonic crystals. In the high-index-contrast material systems that are often necessary for achieving PBG's, the amplitude of the electromagnetic fields falls off sharply away from the defect, resulting in strong photon confinement [4].

Infinite three-dimensional (3-D) photonic crystals have the ability to completely isolate an optical mode from coupling to its surroundings by opening a PBG along every direction in space. The fabrication of three-dimensional crystals, however, poses a great technological challenge. Several different geometries have been suggested for the fabrication of three-dimensional photonic crystals [5]–[9], and three-dimensional PBG's have been measured in the near infrared [10], [11].

Photonic crystals with one-dimensional (1-D) periodicity provide an attractive alternative for achieving strong photon confinement in dielectric structures [12]. Strong three-dimensional confinement can be provided in part by a one-dimensional photonic crystal and in part by the index confinement of a high-dielectric-contrast waveguide. Extending the optical waveguide from both sides of the photonic crystal provides an efficient mechanism for optical coupling into the photonic crystal microcavity, as well as integration into a microphotonics-based device. An active light-emitting structure placed within the microcavity can have enhanced spontaneous emission and could thus be the basis for a low-threshold, high-speed nanolaser.

Unlike infinite 3-D photonic microcavities, light confined in an index-guided structure will couple to radiation modes, and thus have a finite lifetime [13]. Smaller modal volumes in index-guided structures will lead to increased loss into the radiation modes. It is necessary to design these structures carefully to realize a high cavity quality factor (Q), small modal volume, and low losses to radiation modes.

One-dimensional waveguide-based photonic crystals are fabricated in $GaAs/Al_xO_y$ III–V compound semiconductor material waveguide systems, which have the potential for the

0733–8724/99$10.00 © 1999 IEEE

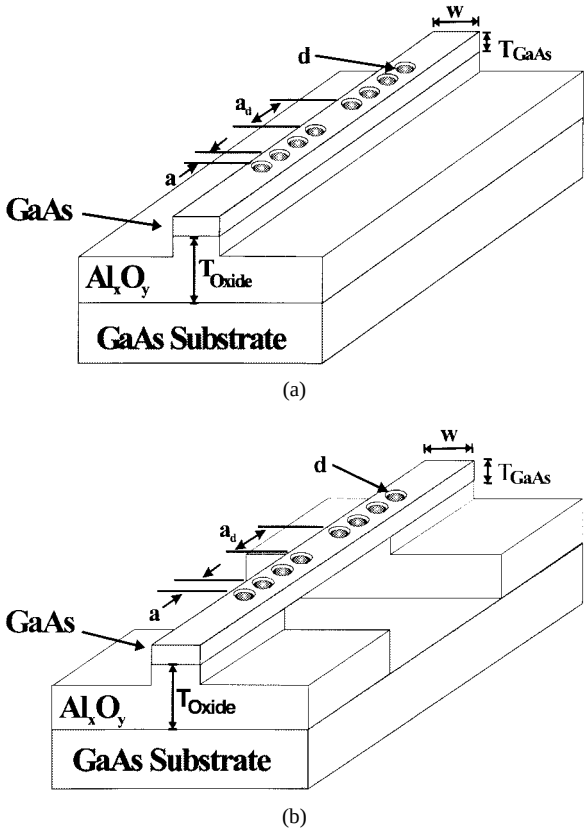

Fig. 1. Schematics of the waveguide microcavities. The GaAs waveguide microcavity is either (a) supported on a low-refractive-index Al_xO_y material (the monorail) or (b) suspended in air (the air-bridge). The 1-D photonic crystal is defined by a periodic array of eight holes; a defect region is created in the crystal by increasing the distance between two holes in the middle of the array.

future integration of active optical devices. Microcavities are made in both monorail and air-bridge geometries. Monorail geometry devices, with an oxide layer remaining intact under the photonic crystal hole arrays, have been studied previously in the GaAs/Al_xO_y material system [14] and with Si/SiO_2 [15] and are easier to fabricate than air-bridge structures. Air-bridge devices are shown to have higher Q's than monorail devices for a given modal volume because of their increased optical confinement. Optical transmission spectra through the microcavities are numerically simulated and experimentally studied. Cavity Q's as high as 360 have been observed near a wavelength of 1.55 μm, and a modal volume as small as 0.026 μm^3 has been calculated. One-dimensional PBG waveguide microcavities have been studied in other geometries [16], [17].

II. Theory

A dielectric waveguide is used to confine light along two dimensions, while a 1-D photonic crystal is used to confine light along the third. The photonic bandgap microcavities are studied in two configurations, namely, the monorail [see Fig. 1(a)] and the air-bridge [see Fig. 1(b)] structures. In both cases, the photonic crystal is defined by an array of eight holes through the waveguide. A change of lattice spacing between the two center holes creates an optical microcavity. In the monorail geometry, the microcavity resides on a low refractive index Al_xO_y material, while in the air-bridge geometry, the microcavity is suspended in air.

A schematic of the supporting monorail waveguide, without any photonic crystal, and the guide's dispersion relations are shown in Fig. 2(a) and (b). The solid lines correspond to the guided modes. The modes are labeled TE-like (electric field primarily parallel to the substrate) and TM-like (electric field perpendicular to the substrate). This labeling convention was chosen despite the fact that TE and TM modes are not strictly defined in strip waveguides with strong field confinement. Quantum wells located at the center of the waveguide could be designed such that light from the wells would couple only to the TE-like modes. The shaded region represents the continuum radiation modes. The slope of the light line is determined by the refractive index of the underlying low-index layer.

The band structure shown in Fig. 2(b) is continuous; there is no upper bound on the wavevector. The introduction of a periodic array of holes into the waveguide has the effect of limiting the wavevector, folding the dispersion relation into the first Brillouin zone, and splitting the guided-mode bands, as shown in Fig. 2(c) and (d). These bands correspond to guided modes, which exist in spite of the presence of holes.

When a defect is introduced in the periodic array of holes, as in Fig. 1(a) and (b), a resonant state can be created inside the bandgap. This defect state, which is a superposition primarily of guided modes, is strongly confined within the defect area. The modal volume V_m is defined to be

$$V_m = \frac{\int \varepsilon \boldsymbol{E}^* \cdot \boldsymbol{E} d^3\boldsymbol{r}}{(\varepsilon \boldsymbol{E}^* \cdot \boldsymbol{E})_{\max}} \tag{1}$$

where ε is the dielectric constant, $\varepsilon \boldsymbol{E}^* \cdot \boldsymbol{E}$ is the energy density in the electric field, and $(\varepsilon \boldsymbol{E}^* \cdot \boldsymbol{E})_{\max}$ is the peak value of $\varepsilon \boldsymbol{E}^* \cdot \boldsymbol{E}$. Using this definition, the minimum modal volume calculated is two times $(\lambda/2n)^3$.

Two competing decay mechanisms contribute to the overall decay rate of the defect state: coupling to guided modes in the waveguide (the desired decay mechanism) and coupling to radiation modes. Controlling the coupling between the defect mode and the radiation continuum is necessary to allow efficient coupling into guided modes. The total quality factor of the resonant mode Q_{tot} is a measure of the optical energy stored in the microcavity over the total cycle-average power radiated out of the cavity. Q_{tot} is defined as $\lambda/\Delta\lambda$, where $\Delta\lambda$ is the width of the resonance and λ is the peak wavelength of the resonance, and obeys [18]

$$\frac{1}{Q_{\text{tot}}} = \frac{1}{Q_{\text{wg}}} + \frac{1}{Q_{\text{rad}}} \tag{2}$$

where $1/Q_{\text{wg}}$ is a measure of the coupling to waveguide modes and $1/Q_{\text{rad}}$ is a measure of the coupling to radiation modes. A finite-difference time-domain computational scheme [19] was used to compute Q_{tot} and the transmission through the structure. Typical results are shown in Fig. 3(a) for monorails and Fig 3(b) for air-bridge microcavities. In both cases, the computation shows a wide bandgap from 1400 to 1700 nm and a sharp resonant peak near 1550 nm.

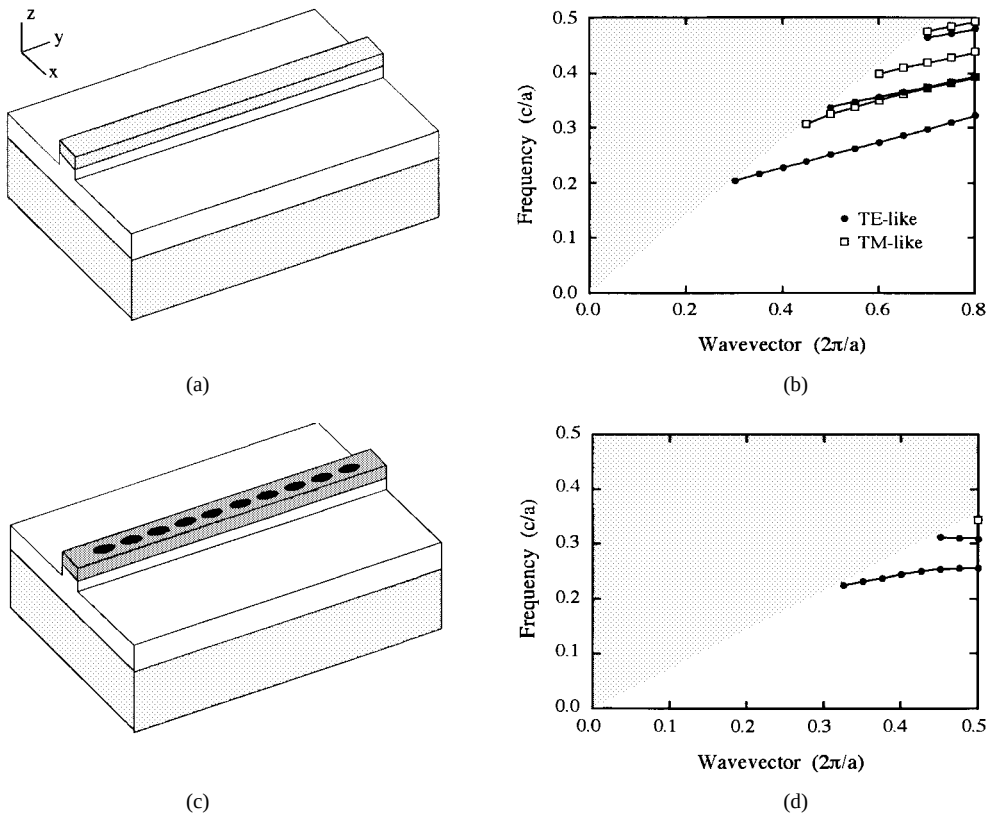

Fig. 2. (a) Schematic diagram of a high-index strip waveguide $(n = 3.48)$ on a low-index layer $(n = 1.44)$. The waveguide has dimensions $0.4a \times 1.2a$ and is single mode over a wide frequency range. (b) Band diagram of the waveguide shown in (a). The solid lines correspond to the guided modes; the shaded region corresponds to the continuum of radiation modes. (c) Schematic diagram of a strip waveguide with a 1-D array of holes of radius $0.23a$. The parameters of the waveguide are identical to those in (a). (d) Band diagram for the waveguide shown in (c). Guided modes do not exist above the cutoff frequency of $0.35c/a$.

Transmission outside the gap is large, which suggests that the modes remain guided as they propagate through the holes, and undergo little scattering. On resonance at 1550 nm, both the monorail and the air-bridge microcavity devices exhibit high transmission. The coupling from the waveguide mode to the cavity resonant mode occurs via the evanescent field through the array of holes. By increasing the number of holes, the reflectivity of the hole array is increased. However, as the number of holes increases, the radiation losses also increase, and thus the throughput of the microcavity decreases. The peak transmission through the cavity is given by

$$T_{\max} = \frac{Q_{\text{tot}}^2}{Q_{\text{wg}}^2}. \tag{3}$$

Because Q_{rad} is finite in the structures, it is not possible to increase the mode confinement and Q_{tot} independently. As the mode confinement increases, coupling to radiation modes also increases, and eventually dominates over coupling to guided modes inside the waveguide. Moreover, the material upon which the microcavity rests provides a favorable escape route for radiation loss. Radiation loss can therefore be minimized in air-bridge microcavities compared to monorail microcavities by removing the underlying material. By increasing the modal volume of the localized state, the coupling to radiation modes reduces (i.e., Q_{rad} increases) and, provided that the coupling to guided modes remains largely unchanged, Q_{tot} as well as $T_{\max}$ increase. Some reduction in Q_{tot} was tolerated in order to achieve high $T_{\max}$, with small modal volume. Q_{tot} can be made greater with larger modal volume designs.

Altering the dimensions of the features in the microcavity structure affects the positions of the band edges and the resonant wavelengths in the transmission spectra. For example, lengthening the defect region will increase the resonant wavelength of a microcavity, and an increase in the thickness of the waveguide primarily shifts the band edges to longer wavelengths. The high-index waveguide provides strong field confinement in the vertical and lateral dimensions such that the guided modes extend only weakly outside the waveguide, allowing a large fraction of the guided modes to interact with the photonic crystal. Strong field attenuation through the array of holes is necessary to achieve small modal volumes.

By coupling an optical emitter to the microcavity resonance, the spontaneous emission rate can be enhanced by a maximum factor of η compared to the rate without a cavity. The expression for η is given as [20]

$$\eta = \frac{Q_{\text{tot}}}{4\pi V_m}\left(\frac{\lambda}{n}\right)^3 \tag{4}$$

where λ is the optical transition wavelength. A number of averaging factors must be taken further into account to find the actual spontaneous emission enhancement for a specific emitter placed within the cavity [21]. For the air-bridge waveguide microcavity that has been measured, the maximum enhancement is calculated to be 72, which is significantly

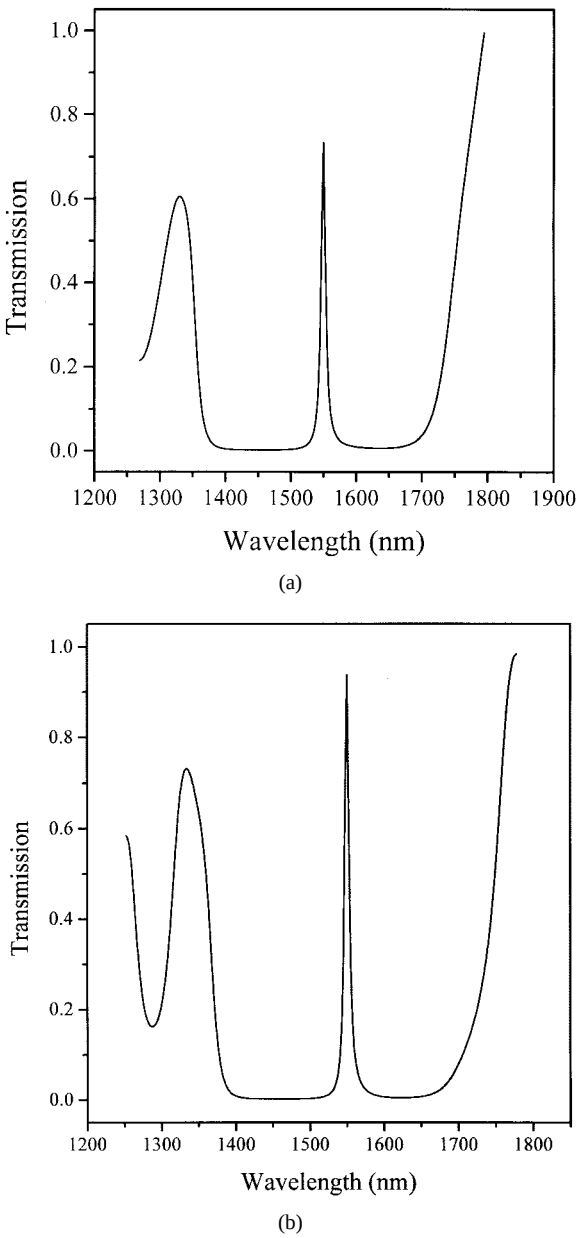

Fig. 3. Theoretical transmission through a PBG (a) monorail and (b) air-bridge microcavity. At the resonance wavelength, a maximum of 72% of the input intensity is transmitted for the monorail microcavity with a cavity $Q_{\rm tot}$ of 200. The air-bridge microcavity exhibits 94% peak transmission and a $Q_{\rm tot}$ of 320.

larger than any enhancement yet measured. This large spontaneous emission enhancement could lead to faster modulation of optical devices and to the development of zero-threshold lasers.

III. Material Issues

High-dielectric constant waveguide systems allow light to be tightly confined and enable photonic crystals to be made with large PBG's. Furthermore, in high-dielectric contrast systems, cavity modes with small modal volumes can be created. The thermal oxidization of AlGaAs layers with high Al content into Al_xO_y provides the necessary dielectric contrast for the operation of GaAs-based photonic crystals; the difference in the index of refraction between the two materials is approximately 1.6.

The process of thermally oxidizing high Al composition AlGaAs layers into Al_xO_y has been implemented in a variety of devices [22]–[26]. For instance, incorporating Al_xO_y current confinement layers into vertical cavity lasers has led to a significant improvement in performance [24]–[26]. In the 1-D PBG crystals fabricated, Al_xO_y was used to provide optical mode confinement and to prevent the loss of light through the GaAs substrate.

For the successful fabrication of photonic devices utilizing Al_xO_y, the lateral and vertical oxidization rates as well as index of refraction have been determined. By oxidizing three $Al_{0.93}Ga_{0.07}As$ layers, each approximately 2 μm thick, for 10, 20, and 30 min, respectively, the vertical oxidization rate was determined to be $\sim$5 μm/h. The lateral oxidation rate of a 1-μm-thick $Al_{0.9}Ga_{0.1}As$ layer was measured to be approximately 4 μm/h; the $Al_{0.9}Ga_{0.1}As$ layer was placed between a 0.5-μm-thick GaAs cap layer and the GaAs substrate. The discrepancy in the vertical and lateral oxidization rates is attributed to the difference in the Al compositions of the AlGaAs layers, as the AlGaAs oxidization rate is known to be highly sensitive to the Al mole fraction [27]. In all cases, the AlGaAs oxidization was performed in a single zone, quartz tube furnace that was maintained at 435 °C. Steam was introduced into the furnace by flowing N_2 at a rate of $\sim$2 l/min through a water bubbler that was maintained at 90 °C. The oxidization time was defined as the time that the sample was exposed to the steam. Further details of the characterization process for the thermal oxide are documented in [28].

The refractive index of Al_xO_y was determined from the reflectance spectrum of a GaAs/Al_xO_y distributed Bragg reflector (DBR). The DBR structure was created by thermally oxidizing four pairs of 115-nm-thick GaAs and 388-nm-thick $Al_{0.92}Ga_{0.08}As$ layers. The reflectance spectra were measured using Fourier-transform infrared spectroscopy. By fitting the reflectance spectra of the DBR prior to and after the oxidization process, the inferred Al_xO_y index of refraction is 1.61, which is comparable to the values reported in the literature [29], [30].

IV. Device Design

The monorail and air-bridge microcavity devices use a GaAs waveguide residing on a layer of Al_xO_y, as shown schematically in Fig. 1(a) and (b). To provide mode confinement in the GaAs waveguide and to prevent optical losses into the substrate, the Al_xO_y layer thickness was designed to be $\sim$2.5 μm. To improve the stability of the oxide, the AlGaAs composition was chosen to be $Al_{0.9}Ga_{0.1}As$ as opposed to pure AlAs [31]. The GaAs waveguide dimensions were $\sim$550 nm wide and $\sim$200 nm thick to obtain a single-mode waveguide. The dimensions depended upon the exact nature of the desired photonic crystal. The waveguides extend 0.5–0.75 mm on both sides of the photonic crystal for efficient coupling into and out of the microcavity, and the waveguides' widths were flared to 3 μm over a distance of 100 μm near the input facet to improve coupling of light into the waveguides. The photonic crystal

TABLE I
DEVICE DIMENSIONS FOR THE MEASURED MONORAIL AND AIR-BRIDGE DEVICES

		Monorail Devices			Airbridge Devices			
		1	2	3	1	2	3	4
Al content of the AlGaAs‡ (%)	x	93	93	93	94	94	94	93
Al_xO_y thickness‡ (μm)	T_{oxide}	2.9	2.9	2.9	2.6	2.6	2.6	3.0
GaAs waveguide thickness‡ (nm)	T_{GaAs}	181	181	181	214	214	214	185
GaAs waveguide width (nm)	w	615*	605*	590*	593	593	525	522
Hole Spacing (nm)	a	420*	420*	410*	500	500	439	439
Hole Diameter (nm)	d	175*	150*	165*	230	230	189	201
Defect Size (nm) (Hole center to Hole center)	a_d	605*	635*	645*	632	703	610	615
Measured Q_{tot}		136	142	117	310	336	*NA*	230
Resonance Wavelength (nm)		1522	1536	1566	1521	1576	*NA*	1512

* Values measured by scanning electron micrograph (SEM).
‡ Values measured by ex-situ variable angle spectroscopic ellipsometry.
All other dimensions are design parameters, and have not actually been measured.

dimensions were varied from device to device to control the PBG and resonance wavelengths while maintaining small modal volumes and high peak transmission. These constraints set a limit on the Q's of the devices. Table I shows the dimensions and layer thicknesses of the monorail and air-bridge microcavity devices discussed in this paper.

V. DEVICE FABRICATION

The fabrication of the monorail and air-bridge microcavity devices consisted of gas source molecular beam epitaxy (GSMBE) deposition of the III–V materials, electron-beam lithography, reactive ion etching (RIE), a plasma-enhanced chemical vapor deposition (PECVD) of SiO_2, AlGaAs thermal oxidization, and wet chemical etching. A schematic depicting the fabrication process sequence is shown in Fig 4.

The AlGaAs and GaAs layers were deposited on a GaAs substrate by GSMBE at 670 and 600 °C and at rates of 1 and 0.3 μm/h, respectively. Using *ex-situ* variable-angle spectroscopic ellipsometry, the thickness and Al content of the AlGaAs layer were measured to be 3 μm and 93 $\pm$ 1%, respectively. The GaAs layer thickness was similarly measured to be 185 $\pm$ 1 nm for the monorail structure and 181 $\pm$ 1 nm for the air-bridge structure.

A 100-nm-thick SiO_2 layer was deposited on the GaAs/$Al_{0.93}Ga_{0.07}As$ heterostructure at 250 °C using PECVD and was followed by spinning on a 200-nm-thick layer of positive electron-beam resist, polymethylmethacrylate (PMMA). The devices were then patterned in the PMMA using direct-write electron-beam lithography. Sixteen electron-beam exposure fields, each approximately 100 $\times$ 100 μm^2, were stitched end-to-end in order to form the overall device structure. After the exposed resist was developed in a 2:1 mixture of 2-propanol and methyl isobutyl ketone at 20 °C for 90 s, a 30-nm-thick layer of nickel was deposited on the sample by electron-beam evaporation. A subsequent liftoff of the nickel film resulted in the image reversal of the electron-beam written patterns [Fig. 4(b)]. Thereafter, the nickel film acted as a mask for the etching of the SiO_2 layer by RIE using a CHF_3/O_2 plasma. After the RIE process, the nickel mask was stripped off with a commercial etchant, and the sample was backside-lapped down to approximately 150 μm.

An RIE process using a $BCl_3/SiCl_4$ plasma transferred the device patterns in the SiO_2 mask into the

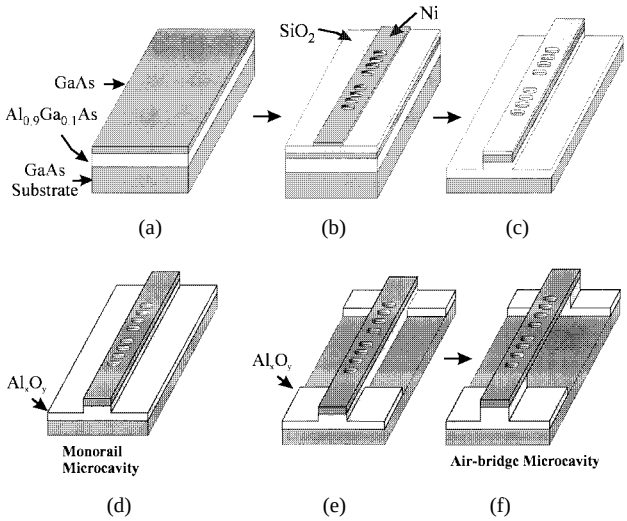

Fig. 4. Fabrication process of the 1-D PBG monorail and air-bridge microcavities. (a) Starting material. (b) After image reversal of patterns that were generated by direct-write electron-beam lithography. (c) After reactive ion etching of the GaAs/$Al_{0.93}Ga_{0.07}As$ heterostructure. (d) Completion of fabrication process for the monorail microcavity after the thermal oxidation of $Al_{0.93}Ga_{0.07}As$ material and facets cleavage. (e) After removal of trench material by reactive ion etching; trench pattern is defined by photolithography. (f) Completion of fabrication process for the air-bridge microcavity after thermal oxidation of $Al_{0.93}Ga_{0.07}As$, photolithographic patterning of the trench area, sacrificial etch of Al_xO_y, and facets cleavage.

GaAs/$Al_{0.93}Ga_{0.07}As$ heterostructure [Fig. 4(c)]. The RIE process etches through the top GaAs layer and about 400 nm into the $Al_{0.93}Ga_{0.07}As$ layer. The process sequences for the monorail and the air-bridge microcavities diverged at this point. For the monorail microcavity, the SiO_2 mask layer was then removed by RIE, and the sample was oxidized for 30 min using the furnace and procedure described above. The holes are thought to extend into the oxidized layer. The extension into the Al_xO_y is not thought to affect the measured Q_{tot}.

For the air-bridge microcavity, a photolithography step was performed to define a 10-μm-wide trench pattern with the photonic crystal in the center of the trench. An RIE step then etches an additional 800 nm into the $Al_{0.93}Ga_{0.07}As$ layer in order to define the trench region and remove the bulk of the sacrificial material. The resist and the SiO_2 mask were then removed using RIE [Fig. 4(e)]. Thereafter, the $Al_{0.93}Ga_{0.07}As$ layer was oxidized using the same procedure as for the monorail structure. Another photolithography step was performed to redefine the same 10-μm-wide trench pattern. The sample was then dipped into a diluted hydrofluoric acid (HF) solution of 10 ml HF:250 ml deionized water that selectively etched the Al_xO_y beneath the photonic crystal, hence suspending the air-bridge structure [Fig. 4(f)]. The sample was immediately rinsed in a sequence of water, methanol, acetone, and methanol to remove the resist. Methanol was used as the final rinsing liquid to prevent the occurrence of stiction by virtue of the lower surface tension of methanol as compared to water.

Last, the facets to the input and output waveguides in both the monorail and air-bridge structures were cleaved to facilitate the coupling of light into the devices during optical characterization. Scanning electron micrographs of both the

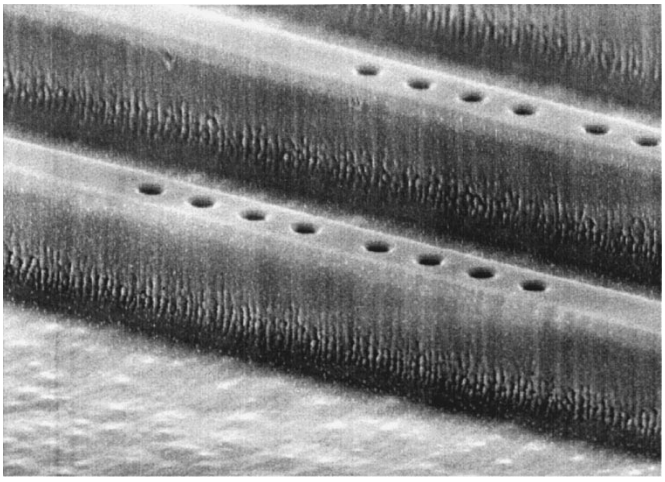

(a)

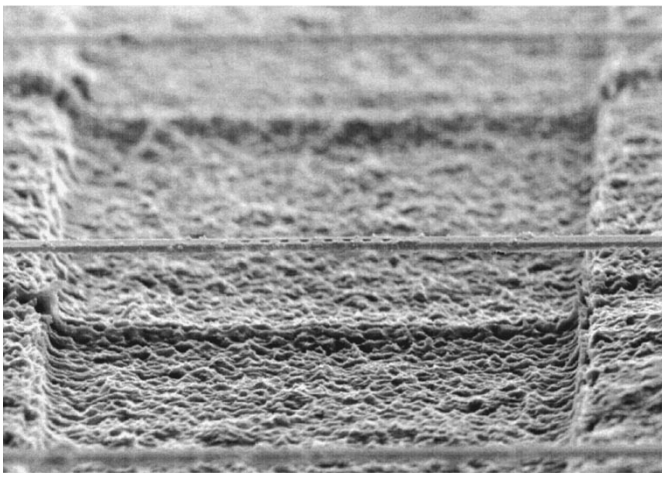

(b)

Fig. 5. Scanning electron micrograph of (a) a monorail microcavity and (b) an air-bridge microcavity. Both geometries have eight holes in the center of the waveguides forming the photonic crystal lattices. (b) Three waveguides are shown running from left to right; the center waveguide is in focus, and the waveguides in the foreground and background are out of focus. The waveguides are suspended over a 10-μm-wide trench of Al_xO_y material. The center-to-center separation between the middle two holes is different from sample to sample to form microcavities with different resonance wavelengths.

monorail and air-bridge microcavity structures are shown in Fig. 5(a) and (b), respectively.

VI. Optical Characterization

Transmission spectra of the devices were studied using the continuous-wave output of an NaCl:OH^- laser. The laser wavelength was tuned with a birefringent plate on a rotary stepper stage, which provided a tuning range from 1500 to 1680 nm and a linewidth of approximately 0.1 nm. The maximum average power was ~250 mW. Wavelength tuning techniques were used to average over ~5 scans/min, with ~45 data points/nm of tuning. The laser light was coupled into an optical fiber, and 3% of that was coupled to a power detector to monitor the laser power. The remaining light was coupled into a waveguide device through a fiber-lens assembly. Polarization was controlled with a polarizing beam splitter cube, a half-wave plate, and a quarter-wave plate, all placed before the

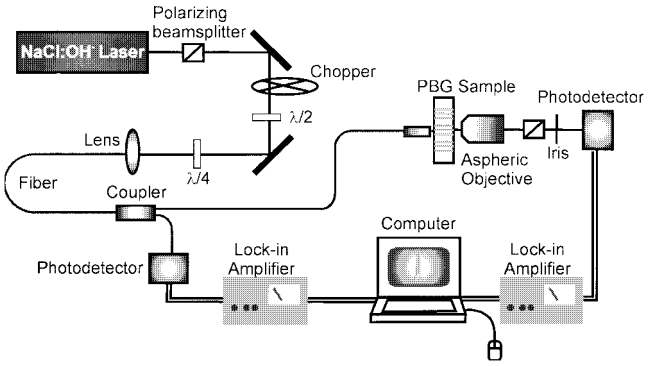

Fig. 6. Schematic diagram showing the experimental setup used to study optical transmission spectra.

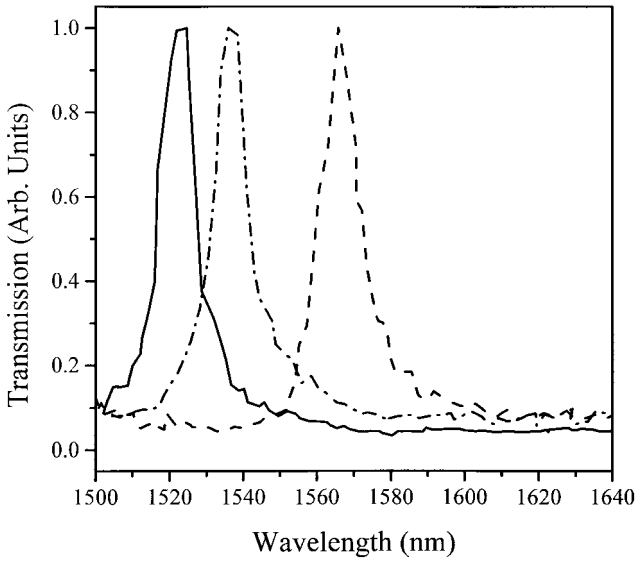

Fig. 7. Transmission spectra through three monorail devices. Each monorail has a different defect length, resulting in different transmission peak wavelengths. The maximum transmission of each peak is normalized to unity.

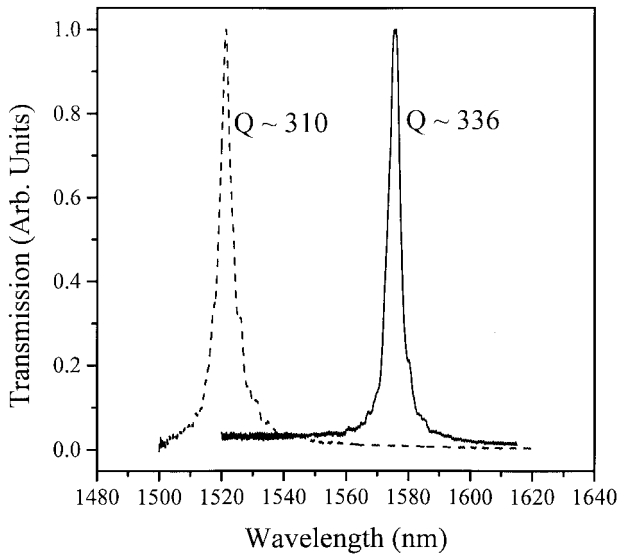

Fig. 8. Transmission spectra measured through two different PBG air-bridge microcavities. The long and short wavelength resonances have defect center-to-center lengths of 632 and 703 nm, respectively. The maxima of the resonance peaks are normalized to unity.

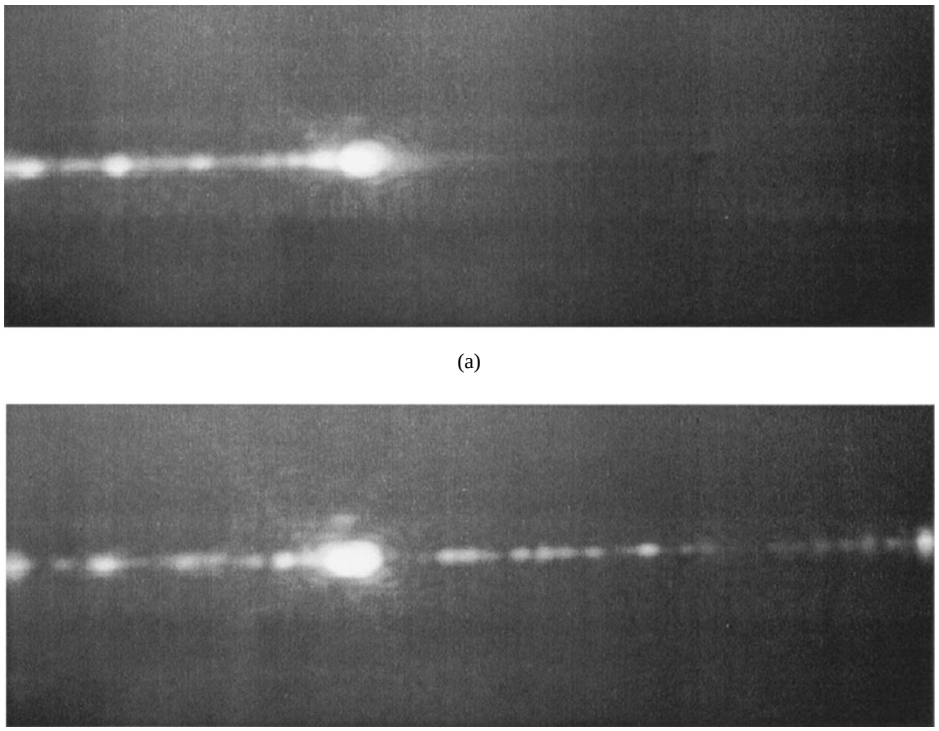

(a)

(b)

Fig. 9. Top view of an illuminated air-bridge microcavity resonator. (a) Off resonance and within the bandgap; the photonic crystal reflects the light. (b) On resonance; light is transmitted through the microcavity resonator. The light is scattered out of the waveguides primarily from surface roughness and is viewed with an infrared camera.

fiber-lens assembly. All measurements were taken with TE polarization, as TM light was not guided. The output of the waveguide was imaged with either a microscope objective or an aspheric lens through a 100-μm pinhole in order to suppress substrate-guided light. A photodetector was placed after the pinhole to monitor the output power, and the wavelength was recorded using an optical spectrum analyzer. Both the input and output power were measured with lock-in detection. A schematic of the experimental setup is shown in Fig. 6.

The losses through straight waveguides without a photonic crystal were estimated to be 3–6 dB/mm by imaging the top of the waveguide with an infrared camera. The intensity of the light scattered out of the waveguide as a function of position can be used to estimate the linear loss. The dominant loss mechanisms appeared to be scattering from sidewall roughness and the GaAs/Al_xO_y interface, which are both accentuated by the tight optical confinement in the high-dielectric-contrast waveguide system. The sidewall roughness resulted from the roughness on the mask that was transferred to the GaAs waveguide. The GaAs/Al_xO_y interface roughness results from the AlGaAs layer growth and oxidation. Other possible loss mechanisms include the error in aligning two successive electron-beam lithography fields together and the intrinsic material loss of the waveguide material at 1.55 μm. At high input powers, two-photon absorption has also been observed. Two-photon absorption excited photoluminescence from the GaAs waveguide was observed by an Si-CCD array camera. Based on the total estimated loss, waveguide input coupling efficiencies of $\sim$3% were calculated.

Optical transmission through several monorail and air-bridge microcavity devices has been measured. Transmission spectra of three different monorail microcavities (monorail devices 1–3 in Table I) are shown in Fig. 7. Each device had a different defect length (defined as the distance between the centers of the holes neighboring the defect region). As expected, larger defect lengths support longer wavelength resonant modes. The cavity modes had cavity Q's of 136, 142, and 117, respectively. The slight increase in transmission at the long wavelength edge may be the beginning of the long wavelength band edge. Due to the lack of a precise loss measurement and the lack of a full band edge within the experimental window, the maxima of the peaks in Fig. 7 were normalized to unity rather than to the absolute transmission.

The normalized experimental transmissions through two distinct air-bridge microcavities (air-bridge devices 1 and 2 in Table I), having defect center-to-center lengths of 632 and 703 nm, respectively, are shown in Fig. 8. The resonance states had Q's of 310 and 336, respectively. Resonance Q's as high as 360 have been recorded in air bridge device 2. As in the case of the monorail waveguides, the resonance shifted to longer wavelengths as the microcavity size was increased. Because the PBG was calculated to be over 300 nm wide, the band edges were not visible within the 180-nm tuning range of the laser. The plots in Fig. 8 were normalized by

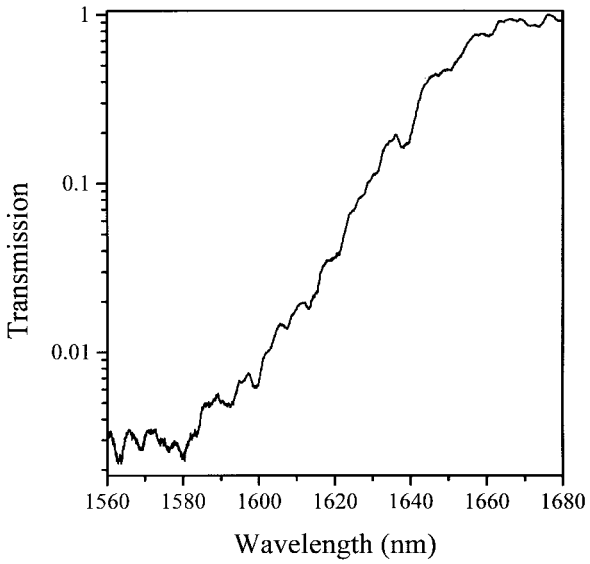

Fig. 10. Transmission spectrum of a PBG air-bridge sample where the long wavelength band edge has been shifted into the experimentally accessible wavelength range. The band edge is shown on a log plot and exhibits a 27-dB suppression of transmission within the bandgap compared to outside the bandgap.

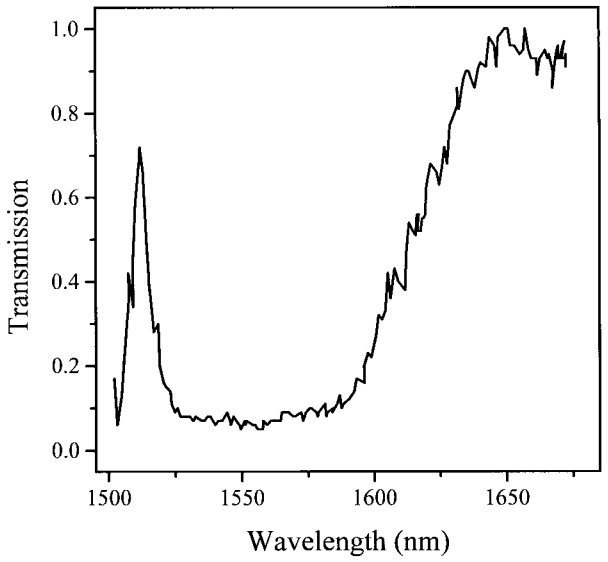

Fig. 11. Transmission spectrum of an air-bridge microcavity exhibiting both a resonance and a band edge within the experimentally accessible wavelength range. Transmission outside the bandgap is normalized to unity, revealing 72% relative transmission on resonance, with a cavity Q of 230.

the same method as the monorail structures in Fig. 7. Both of the transmission spectra in Fig. 8 were averages of ten scans taken back-to-back and had a wavelength resolution close to the laser bandwidth. Air-bridge device had a modal volume of 0.031 μm^3. Smaller modal volumes are predicted to lead to increased loss due to radiation modes in waveguide-based devices. However, the air-bridge microcavities have higher Q's than monorail microcavities of the same modal volume because of the increased isolation of the resonance mode from substrate radiation modes. Using a modal volume of 0.031 μm^3, a Q of 310, and a peak wavelength of 1521 nm, the maximum enhancement factor for spontaneous emission from such a defect is computed to be $\eta = 72$.

A top-view image of an illuminated microcavity is shown in Fig. 9. This picture was taken with an infrared camera. Some of the light being transmitted by the waveguide was scattered by surface roughness and was visible to the camera. Off resonance, the light stopped at the photonic crystal located in the center of the guide and was reflected as shown in Fig. 9(a). On resonance, the incident light was transmitted, and the portion of the waveguide after the photonic crystal was illuminated as shown in Fig. 9(b).

By changing the photonic crystal dimensions, a full photonic band edge was observed within the laser tuning range. One device with a band edge at 1620 nm (air-bridge device 3 in Table I), is shown in Fig. 10. This spectrum was an average of ten scans taken back-to-back and had a wavelength resolution close to the laser bandwidth. The bumpy features on the band edge trace are real and repeatable. This band edge, plotted logarithmically, had $\sim$27 dB attenuation of transmission for wavelengths within the bandgap compared to outside of the bandgap. The transmission floor within the bandgap was a true feature of the device measured and was consistent with theoretical simulations.

A second device (air-bridge device 4 in Table I) exhibited both a band edge and the resonance within the laser tuning window (Fig. 11). Because the band edge and the resonance were both fully visible at the same time, it is possible to determine the transmission of the microcavity resonance relative to that outside of the bandgap. This yielded a maximum relative transmission of 72% on resonance, with a Q of 230. The modal volume of device 4 was calculated to be 0.026 μm^3, which is only 2 $(\lambda/2n)^3$. The lower Q is a result of the resonances being shifted closer to the band edge.

VII. Conclusion

One-dimensional photonic bandgap crystals have the potential to control the propagation and spontaneous emission of light and have applications for efficient, submicrometer scale opto-electronics. Resonant microcavities with small modal volumes will serve as the basis of a low-threshold laser cavity with fast modulation rates. Air-bridge and monorail geometry microcavities with modal volumes as low as 0.026 μm^3 have been designed, fabricated, and measured in 1-D PBG structures. The structures were designed to have high Q's, taking into account the tradeoff between increased optical confinement and increased radiation loss. Waveguide microcavity structures were measured to have Q's as high as 360 in the 1.55-μm regime. Furthermore, the photonic crystals have been fabricated in the GaAs/Al_xO_y III–V compound semiconductor system, which provides the potential for fabrication of active devices and allows integration of photonic crystal and active semiconductor technologies.

Acknowledgment

The authors gratefully acknowledge the contributions of B. Bailey, H. Haus, S. Hoyt, M. Mondol, H. Smith, and G. Steinmeyer.

REFERENCES

[1] H. Yokoyama and K. Ujihara, *Spontaneous Emission and Laser Oscillation in Microcavities*. Boca Raton, FL: CRC Press, 1995.

[2] E. Yablonovitch, "Inhibited spontaneous emission in solid-state physics and electronics," *Phys. Rev. Lett.*, vol. 58, pp. 2059–2062, 1987.

[3] J. D. Joannopoulos, P. R. Villeneuve, and S. Fan, "Photonic crystals: Putting a new twist on light," *Nature*, vol. 386, pp. 143–149, 1997.

[4] J. D. Joannopoulos, R. D. Meade, and J. N. Winn, *Photonic Crystals*. Princeton, NJ: Princeton University Press, 1995.

[5] E. Yablonovitch, T. J. Gmitter, and K. M. Leung, "Photonic band structure: The face-centered-cubic case employing nonspherical atoms," *Phys. Rev. Lett.*, vol. 67, pp. 2295–2298, 1991.

[6] K. M. Ho, C. T. Chan, C. M. Soukoulis, R. Biswas, and M. Sigalas, "Photonic band gaps in three dimensions: New layer-by-layer periodic structures," *Solid State Commun.*, vol. 89, pp. 413–416, 1994.

[7] H. S. Sözüer, and J. P. Dowling, "Photonic band calculations for woodpile structures," *J. Mod. Opt.*, vol. 41, pp. 231–239, 1994.

[8] G. Feiertag, W. Ehrfeld, H. Feimuth, H. Kolle, H. Lehr, M. Schmidt, M. M. Sigalas, C. M. Soukoulis, G. Kiriakidis, T. Pedersen, J. Kuhl, and W. Koenig, "Fabrication of photonic crystals by deep X-ray," *Appl. Phys. Lett.*, vol. 71, pp. 1441–1443, 1997.

[9] S. Fan, P. R. Villeneuve, R. D. Meade, and J. D. Joannopoulos, "Design of three-dimensional photonic crystals at submicron length scales," *Appl. Phys. Lett.*, vol. 65, pp. 1466–1468, 1994.

[10] J. G. Fleming and S.-Y. Lin, "Three-dimensional photonic crystal with a stop band from 1.35–1.95 μm," *Opt. Lett.*, vol. 24, pp. 49–51, 1999.

[11] C. Cheng and A. Scherer, "Fabrication of photonic band-gap crystals," *J. Vac. Sci. Technol. B*, vol. 13, pp. 2696–2700, 1995.

[12] P. R. Villeneuve, S. Fan, J. D. Joannopoulos, K.-Y. Lim, G. S. Petrich, L. A. Kolodziejski, and R. Reif, "Air-bridge microcavities," *Appl. Phys. Lett.*, vol. 67, pp. 167–169, 1995.

[13] P. R. Villeneuve, S. Fan, S. G. Johnson, and J. D. Joannopoulos, "Three-dimensional photon confinement in photonic crystals of low-dimensional periodicity," *Inst. Elect. Eng. Proc. Optoelectron.*, Dec. 1998.

[14] K.-Y. Lim, D. J. Ripin, G. S. Petrich, L. A. Kolodziejski, E. P. Ippen, M. Mondol, H. I. Smith, P. R. Villeneuve, S. Fan, and J. D. Joannopoulos, "Photonic bandgap waveguide microcavities: monorails and air-bridges," *J. Vac. Sci. Technol. B*, vol. 17, no. 3, pp. 1171–1174, 1999.

[15] J. S. Foresi, P. R. Villeneuve, J. Ferrera, E. R. Thoen, G. Steinmeyer, S. Fan, J. D. Joannopoulos, L. C. Kimerling, H. I. Smith, and E. P. Ippen, "Photonic-bandgap microcavities in optical waveguides," *Nature*, vol. 390, pp. 143–145, 1997.

[16] T. F. Krauss, B. Vögele, C. R. Stanley, and R. M. De La Rue, "Waveguide microcavity based on photonic microstructure," *IEEE Photon. Technol. Lett.*, vol. 9, pp. 176–178, 1997.

[17] J. P. Zhang, D. Y. Chu, S. L. Wu, W. G. Bi, R. C. Tiberio, R. M. Joseph, A. Taflove, C. W. Tu, and S. T. Ho, "Nanofabrication of 1-D photonic bandgap structures along a photonic wire," *IEEE Photon. Technol. Lett.*, vol. 8, pp. 491–493, 1996.

[18] H. A. Haus, *Waves and Fields in Optoelectronics*. Englewood Cliffs, NJ: Prentice-Hall, 1984.

[19] K. S. Kunz and R. J. Luebbers, *The Finite-Difference Time-Domain Method for Electronics*. Boca Raton, FL: CRC, 1993.

[20] H. Yokoyama and S. D. Brorson, "Rate equation analysis of microcavity lasers," *J. Appl. Phys.*, vol. 66, pp. 4801–4805, 1989.

[21] J. M. Gérard, B. Sermage, B. Gayral, B. Legrand, E. Costard, and V. Thierry-Mieg, "Enhanced spontaneous emission by quantum boxes in a monolithic optical microcavity," *Phys. Rev. Lett.*, vol. 81, pp. 1110–1113, 1998.

[22] W. T. Tsang, "Self-terminating thermal oxidation of AlAs epilayers on GaAs by molecular beam epitaxy," *Appl. Phys. Lett.*, vol. 33, pp. 426–429, 1978.

[23] J. M. Dallesasse, N. Holonyak, Jr., A. R. Sugg, T. A. Richard, and N. El-Zein, "Hydrolyzation oxidation of $Al_xGa_{1-x}As$-AlAs-quantum well heterostructures and superlattices," *Appl. Phys. Lett.*, vol. 57, pp. 2844–2846, 1990.

[24] G. M. Yang, M. H. MacDougal, and P. D. Dapkus, "Ultralow threshold current vertical-cavity surface-lasers obtained with selective oxidation," *Electron. Lett.*, vol. 31, pp. 886–888, 1995.

[25] K. D. Choquette, R. P. Schneider, K. L. Lear, and K. M. Geib, "Low threshold voltage vertical-cavity lasers fabricated by selective oxidation," *Electron. Lett.*, vol. 30, pp. 2043–2044, 1994.

[26] K. L. Lear, K. D. Choquette, R. P. Schneider, S. P. Kilcoyne, and K. M. Geib, "Selectively oxidized vertical-cavity surface emitting lasers with 50% power conversion efficiency," *Electron. Lett.*, vol. 31, pp. 208–209, 1995.

[27] K. D. Choquette, K. M. Geib, C. I. H. Ashby, B. O. Twesten, H. Q. Hou, D. M. Follstaedt, B. E. Hammons, D. Mathes, and R. Hull, "Advances in selective wet oxidation of AlGaAs alloys," *IEEE J. Quantum Electron.*, vol. 3, pp. 916–926, 1997.

[28] K. Y. Lim, D. J. Ripin, G. S. Petrich, P. R. Villeneuve, S. Fan, J. D. Joannopoulos, E. P. Ippen, and L. A. Kolodziejski, "The role of the thermal oxide in GaAs-based photonic bandgap waveguide microcavities," *Adv. Mater.*, vol. 11, pp. 501–505, 1999.

[29] M. H. MacDougal and P. D. Dapkus, "Wavelength shift of selectively oxidized Al_xO_y-AlGaAs-GaAs Distributed Bragg Reflectors," *IEEE Photon. Technol. Lett.*, vol. 9, pp. 884–886, 1997.

[30] F. A. Kish, S. J. Caracci, N. J. Holonyak, J. M. Dallesasse, K. C. Hsieh, M. J. Ries, S. C. Smith, and R. D. Burnham, "Planar native oxide index guided AlGaAs-GaAs quantum well heterostructure lasers," *Appl. Phys. Lett.*, vol. 59, pp. 1755–1757, 1991.

[31] K. D Choquette, K. M. Geib, R. Hull, H. Q. Hou, K. L. Lear, H. C. Chui, B. E. Hammons and J. A. Nevers, "Wet oxidation of AlGaAs versus AlAs: A little gallium is good," in *Proc. IEEE 1996 LEOS Annu. Meeting*. Piscataway, NJ: IEEE Press, 1996, pp. 390–391.

Daniel J. Ripin, photograph and biography not available at the time of publication.

Kuo-Yi Lim (M'98), photograph and biography not available at the time of publication.

G. S. Petrich (M'92), photograph and biography not available at the time of publication.

Pierre R. Villeneuve, photograph and biography not available at the time of publication.

Shanhui Fan, photograph and biography not available at the time of publication.

E. R. Thoen (S'98), photograph and biography not available at the time of publication.

John D. Joannopoulos, photograph and biography not available at the time of publication.

E. P. Ippen (S'66–M'69–SM'81–F'84), photograph and biography not available at the time of publication.

L. A. Kolodziejski (M'87–SM'97), photograph and biography not available at the time of publication.